



# 1 A Correction Algorithm for Propeller-Induced Airflow 2 and Flight Attitude Changes during Three- 3 Dimensional Wind Speed Measurements Made from A 4 Rotary Unmanned Aerial Vehicle

5 Yanrong Yang<sup>1+</sup>, Yuheng Zhang<sup>1+</sup>, Tianran Han<sup>1</sup>, Conghui Xie<sup>1</sup>, Yayong Liu<sup>1</sup>, Yufei  
6 Huang<sup>1</sup>, Jietao Zhou<sup>1</sup>, Haijiong Sun<sup>1</sup>, Delong Zhao<sup>2</sup>, Kui Zhang<sup>3</sup>, Shao-Meng Li<sup>1\*</sup>

7 <sup>1</sup>College of Environmental Sciences and Engineering, Peking University, Beijing 100871, China

8 <sup>2</sup>Beijing Weather Modification Center, Beijing 100089, China

9 <sup>3</sup>Beijing Wisdominc Technology Co., Ltd, Beijing 100070, China

10 <sup>+</sup>Contributed equally to the work

11 *Correspondence to:* Shao-Meng Li (shaomeng.li@pku.edu.cn)

12 **Abstract.** A hexacopter unmanned aerial vehicle (UAV) was fitted with a three-dimensional sonic  
13 anemometer to measure three-dimensional wind speed, air temperature, relative humidity, and pressure.  
14 To obtain accurate results for three-dimensional wind speeds, we developed an algorithm to correct  
15 biases caused by the propeller-induced airflow disturbance, UVA movement, and changes in flight  
16 attitude in the three-dimensional wind measurements. The wind measurement platform was built based  
17 on a custom-designed integration kit that couples seamlessly to the UAV, equipped with a payload and  
18 the sonic anemometer. Based on an accurate digital model of the integrated UAV-payload-anemometer  
19 platform, computational fluid dynamics (CFD) simulations were performed to quantify the wind speed  
20 disturbances caused by the rotation of the UAV's rotor on the anemometer during the UAV's steady flight  
21 under headwind, tailwind, and crosswind conditions. Through analysis of the simulated data, regression  
22 equations were developed to predict the wind speed disturbance, and the correction algorithm for rotor  
23 disturbances, motions, and attitude changes was developed. To validate the correction algorithm, we  
24 conducted a comparison study in which the integrated UAV system flew around a meteorological tower  
25 on which three-dimensional wind measurements were made at multiple altitudes. The comparison  
26 between the corrected UAV wind data and those from the meteorological tower demonstrated an  
27 excellent agreement. The corrections result in significant reductions in wind speed bias caused mostly  
28 by the propellers, along with notable changes in the dominant wind direction and wind speed in the  
29 original data. The algorithm enables reliable and accurate wind speed measurements in the atmospheric  
30 boundary layer made from rotorcraft UAVs.



31 **Keywords:** UAV; Propeller Disturbance; Three-dimensional Wind; Correction Algorithm

## 32 **1 Introduction**

33 Wind measurement is crucial in various fields of research and application, including meteorology and  
34 environmental sciences. Accurate wind characteristics facilitate modeling of atmospheric transport  
35 patterns (Gryning et al., 1987; Stockie, 2011), remote sensing data verification (Drob et al., 2015), model  
36 input data assimilation (Gousseau et al., 2011; Vardoulakis et al., 2003) and digital modeling result  
37 optimization (Booij et al., 1999; Van Hooff and Blocken, 2010). In particular, wind profile measurements  
38 near surface can improve the understanding of atmospheric boundary layer (ABL) dynamics and  
39 micrometeorological turbulence at the surface (Seibert et al., 2000), allowing detailed understandings  
40 and model description of energy and mass exchanges between air and surfaces and transport processes.

41 The recent development of unmanned aerial vehicles (UAVs) has provided an opportunity for the  
42 measurement of wind fields in three dimensions with high spatial resolutions (Mcgonigle et al., 2008;  
43 Martin et al., 2011; Kim and Kwon, 2019). The small size, low flight altitude, high mobility and ability  
44 to assemble sensing devices make UAVs ideal platforms from which to measure wind in the ABL  
45 (Thielicke et al., 2021; Shaw et al., 2021; Stewart et al., 2021). Multirotor UAVs allow flexible control  
46 of flight attitude and stationary hovering, and can carry varying payloads depending on the number of  
47 rotors (Villa et al., 2016; Riddell, 2014; Bonin et al., 2013; Stewart et al., 2021), offering significant  
48 advantages in capturing high-resolution wind characteristics in low-altitude conditions (Anderson and  
49 Gaston, 2013; Mcgonigle et al., 2008).

50 UAVs are often employed to measure wind characteristics both directly and indirectly. Indirect  
51 measurement methods involve utilizing pre-installed sensors on the UAV (Elston et al., 2015), in  
52 conjunction with specialized flight patterns and wind retrieval algorithm (Bonin et al., 2013; Rautenberg  
53 et al., 2018; Gonzalez-Rocha et al., 2019) to achieve wind speed measurement. Although this method is  
54 straightforward to operate, it does not accurately reflect actual wind conditions during flight. Direct  
55 measurement methods entail installing additional wind sensors on the UAV to obtain real-time wind  
56 information in the field. Porous probes (Soddell et al., 2004; Spiess et al., 2007), pitot tubes (Niedzielski  
57 et al., 2017; Langelaan et al., 2011), and anemometers (Rogers and Finn, 2013; Nolan et al., 2018) are  
58 commonly used sensors. Sonic anemometers are a more prevalent choice for rotorcraft UAVs, capable



59 of measuring wind speed by detecting changes in the speed of sound travel between different  
60 sensors(Thielicke et al., 2021). Due to the increasing use of rotorcraft UAVs for wind measurements,  
61 sonic anemometers are recognized as one of the most promising methods in terms of measurement  
62 accuracy and precision.

63 Sonic anemometers have been mounted onto rotary-wing UAVs for measuring wind speed to varying  
64 degrees of success. Typically, an anemometer is mounted at a position along the central axis above the  
65 UAV, with data adjusted for the additional wind speed signals induced by UAV motion and attitude  
66 changes. Nevertheless, the strong airflow perturbations caused by the rotating propellers can distort real  
67 wind flow patterns and significantly affect the accuracy of wind measurements (De Divitiis, 2003).  
68 However, these distortions were not considered in the adjustment algorithms. To address this issue,  
69 researchers have developed several new correction methods. The first method involves mounting the  
70 anemometer along the central axis high above the UAV where the rotor wash effects are believed to be  
71 limited on the wind speed measurement (Shimura et al., 2018; Barbieri et al., 2019). However, it may  
72 not be suitable for hexacopters and octocopters due to the high position required, which may raise safety  
73 and flight control concerns. The second method involves new corrections based on experiments in an  
74 indoor area to measure wind velocity signal bias caused by the rotors during flight and then subtracting  
75 the bias (Palomaki et al., 2017). However, this method is limited by the size of the indoor area,  
76 inadequate for full simulations of real UAV rotor speed and attitude changes during flight, and  
77 insufficient for the development of a comprehensive correction scheme. Additionally, it does not take  
78 into account the detailed coupling of true winds with propeller downwash. The third method is similar  
79 to the second except the use of wind tunnels to establish a more accurate relationship between increased  
80 air speed and UAV motion or attitude parameters (Thielicke et al., 2021; Neumann and Bartholmai,  
81 2015). While effective in determining numerical relationships, the method is limited by the high cost of  
82 wind tunnel experiments, and more importantly, by the additional errors introduced by reflected airflows  
83 from the wind tunnel walls and ground, as well as the same issues of full simulations of real UAV rotor  
84 speed and attitude changes during flight.

85 The flaws in these correction methods could be addressed by using computational fluid dynamics (CFD)  
86 simulations to analyze the airflow generated by the UAV's propellers. As far as we know, CFD has been  
87 employed to analyze airflow patterns around drones but hasn't been utilized to correct wind



88 measurements obtained from UAVs (Oktay and Eraslan, 2020; Hedworth et al., 2022). In this paper, we  
89 introduce a three-dimensional wind speed correction algorithm for sonic anemometer wind  
90 measurements taken from a rotary UAV. This algorithm considers the propeller-induced airflow of the  
91 UAV, based on CFD simulations, along with the UAV's motion and attitude changes during flight. The  
92 accuracy of the algorithm is confirmed by comparing the corrected wind speeds with those measured  
93 from a meteorological tower at multiple altitudes. These results could contribute to ongoing efforts  
94 aimed at enhancing the performance and reliability of UAV-based wind speed measurement techniques.  
95 Additionally, they pave the way for potential applications, such as quantifying pollutant emissions from  
96 industrial complexes (Han T, 2023).

## 97 **2 Method**

### 98 **2.1 Equipment and Digital Model Representation**

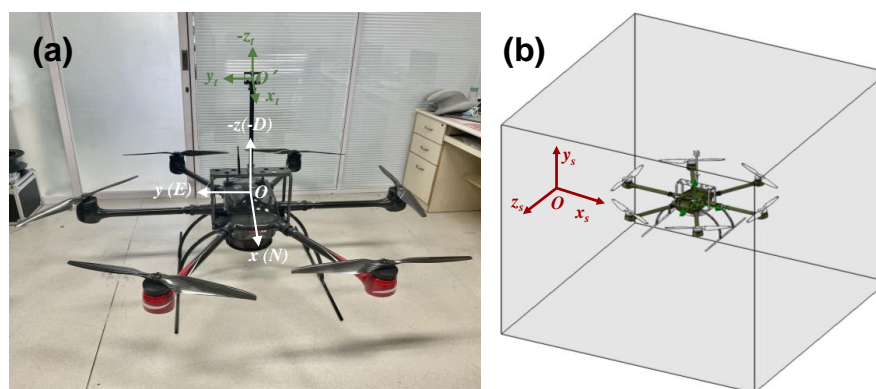
99 A six-rotor UAV (KWT-X6L-15, ALLTECH, China), equipped with six 32 cm diameter propellers  
100 driven by M10 KV100 brushless DC motors, was the platform from which wind was measured. The  
101 UAV has a symmetrical motor wheelbase of 1765 mm with an unloaded takeoff weight of 22.5 kg and  
102 a maximum flight speed of 18 m s<sup>-1</sup>. It has a flight endurance >30 min while carrying its maximum  
103 payload of 15 kg.

104 A miniature three-dimensional ultrasonic anemometer (Trisonica-Mini Wind and Weather Sensor,  
105 Anemoment, America) allowed the measurement of wind speed under 15 m s<sup>-1</sup> with an accuracy of ±  
106 0.1 m s<sup>-1</sup> and a resolution of 0.1 m s<sup>-1</sup>, and wind direction of 0-360° with an accuracy of ± 0.1° and a  
107 resolution of 0.1°. It was set at 70 cm above the plane of the propellers of the UAV, mounted on a custom-  
108 design carbon fiber tube and frame which was further mounted onto a rectangular carbon fiber support  
109 base attached to the underbelly of the UAV body, to minimize the effect of propellers-induced flow on  
110 the anemometer measurement. The  $x_r$ - $y_r$ - $z_r$  coordinate axes of the anemometer, with its center as the  
111 origin, were set to be parallel to the  $x$ - $y$ - $z$  axes of the aircraft body frame. The mounting of the three-  
112 dimensional anemometer is shown in Fig. 1(a).

113 A base digital model of the UAV was provided by its manufacturer for the present CFD simulations. The  
114 digital model was further augmented with the accurate digital representation of the three-dimensional  
115 anemometer and its mounting frame. Furthermore, considering that the UAV wind measurements are



116 usually tied to other air measurement applications, necessitating additional payload attached to the UAV  
117 underbelly simultaneously. Such a payload on the UAV needs also to be included in the digital model  
118 for the CFD simulation. In the present case, we added the digital model of a 6.37 kg air sampler  
119 developed in our group (Han T, 2023) to the UAV base digital model (Fig. 1(b)).  
120 For CFD simulations, the complete digital model for the UAV and its payloads was set in the  $x_s$ - $y_s$ - $z_s$   
121 simulation coordinate system in Solidworks, a computational fluid simulation tool, on a one-to-one scale  
122 (Fig. 1(b)).



123  
124 **Figure 1:** (a) The UAV wind speed measurement platform. (b) The digital model of the UAV wind  
125 measurement platform in the 3D CFD model simulation domain.

## 126 2.2 CFD Simulation Parameters Configuration

### 127 2.2.1 Environmental Parameters

128 Since the UAV's predominant flights are within the atmospheric boundary layer, characterized by  
129 significant variability in wind speed and directions, a flight envelope for the UAV in the simulated  
130 environments was setup for the complete UAV digital model for flight altitudes of 30 meters and 1000  
131 meters, respectively. These flight envelopes were designed for the UAV to subject to headwind, tailwind,  
132 and crosswind relative to its flight direction. Under the constraint that the UAV can only operate under  
133 true wind speeds  $\leq 18 \text{ m s}^{-1}$ , and assuming the applicability of the correction algorithm to most flight  
134 scenarios, CFD simulations were conducted for the UAV under these three wind directions. The  
135 simulations encompassed the following flight envelopes as listed in Table 1: the UAV flew at ground  
136 speeds of 18, 14, 10, and 8  $\text{m s}^{-1}$ , respectively, and adapted to wind speeds of 1.5, 3.3, 5.4, 7.9, 10.7, and  
137 14  $\text{m s}^{-1}$ .



138 **Table 1: Ground speed and wind speed configuration in the presence of tailwind, headwind, and crosswind**  
 139 **conditions relative to the UAV's flight direction.**

Wind Type	Ground Speed (m s <sup>-1</sup> )	Wind speed (m s <sup>-1</sup> )	Wind Type	Ground Speed (m s <sup>-1</sup> )	Wind speed (m s <sup>-1</sup> )	Wind Type	Ground Speed (m s <sup>-1</sup> )	Wind speed (m s <sup>-1</sup> )
		1.5			1.5			1.5
		3.3			3.3			3.3
	8	5.4		8	5.4		8	5.4
		7.9						7.9
		10.7						10.7
								14
		1.5			1.5			1.5
		3.3			3.3			3.3
	10	5.4		10	5.4		10	5.4
		7.9			7.9			7.9
		10.7						10.7
								14
Tailwind		1.5	Headwind		1.5	Crosswind		1.5
		3.3			3.3			3.3
	14	5.4		14	5.4		14	5.4
		7.9			7.9			7.9
		10.7			10.7			10.7
								14
		1.5			1.5			1.5
		3.3			3.3			3.3
	18	5.4		18	5.4		18	5.4
		7.9			7.9			7.9
		10.7			10.7			10.7
								14

140 **2.3 Flight Parameters**

141 The movements of the UAV through air, including takeoff, ascent/descent, attitude changes, turning, and  
 142 horizontal flights, are driven by the rotary propellers, whose power requirement is closely tied to the  
 143 weights of the UAV and its payload as well as the relative motions of the UAV in air. During a normal  
 144 flight, the UAV adjusts its inclination angle and propeller speeds in order to achieve a set ground speed  
 145 for flight. By analyzing the gravity  $G$ , pull  $T$  and wind resistance  $D$  experienced by the UAV under flight  
 146 conditions, its inclination angle  $\theta$  and propeller rotation speed  $M$  can be calculated according to Eqs. (1)-  
 147 (5)(Quan, 2017).



148  $\tan\theta \times mg = D$  (1)

149  $p \times (\sin\theta \times S_{xoy} + \cos\theta \times S_{xoz}) = D$  (2)

150  $0.5\rho(V_{wind} + V_{UAV})^2 = p$  (3)

151  $\cos\theta \times mg = T$  (4)

152  $T = C_T \times \rho \times \left(\frac{M}{60}\right)^2 \times D_p^4$  (5)

153 where  $\theta$  is the inclination angle of the UAV;  $m$  is the combined weight of the UAV and the payloads (i.e.,  
154 the air sampler and the anemometer plus its installation frame in the present case), calculated to be  
155 28.869 kg;  $g$  is the gravitational constant at 9.8 m s<sup>-2</sup>;  $D$  is the wind resistance in Newtons;  $V_{wind}$  is the  
156 wind speed in m s<sup>-1</sup>;  $V_{UAV}$  is the ground speed of the UAV in m s<sup>-1</sup>;  $p$  is the wind pressure on the UAV in  
157 N/m<sup>2</sup>;  $S_{xoy}$  and  $S_{xoz}$  are the projected surfaces of the UAV in the horizontal direction and vertical directions,  
158 determined to be 0.296 and 0.229 m<sup>2</sup>, respectively;  $C_T$  is the rotor pull coefficient with an experimentally  
159 determined value of 0.048542;  $D_p$  is the UAV propeller diameter at 0.8128 m;  $\rho$  is the air density in kg  
160 m<sup>-3</sup>;  $T$  is each rotor pull in Newton;  $M$  is the rotation speed of the rotors in RPM.

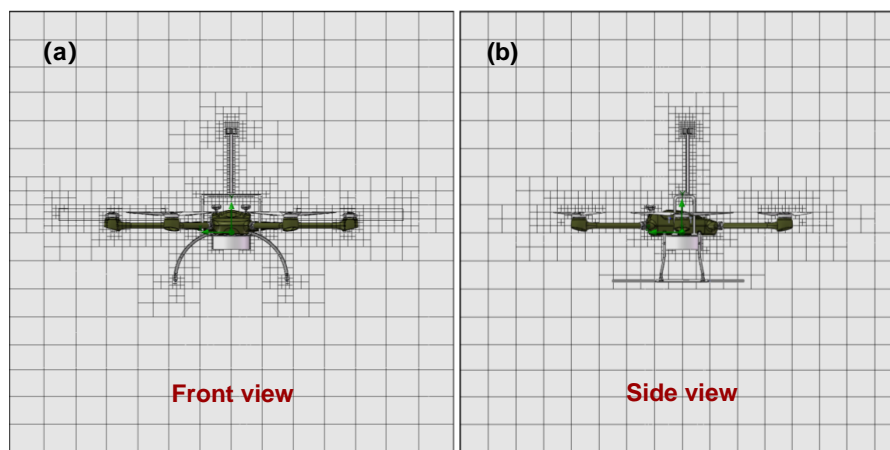
161 The calculated  $M$  values were corrected for the different UAV attitude,  $V_{wind}$ , and  $V_{UAV}$  combinations as  
162 appropriate. Each set of flight condition parameters that constitute the full flight envelope, including  
163 wind directions, wind speeds, airspeeds, ground speed, inclination, wind resistance, pull,  $M$  and  
164 corrected  $M$  are given in Table S1 and S2 of Support Information. The CFD simulations were performed  
165 to determine the wind fields for each set of parameters in the flight envelope one at a time.

#### 166 **2.4 Simulation Parameters**

167 During the CFD flow simulations of the UAV using Solidworks, the computational domain was set to  
168 3.3×3.3×3.3 m<sup>3</sup> according to the wingspan of the UAV, with the complete UAV plus payload digital  
169 model set at the center of the domain. The computational domain was divided into two parts with  
170 different spatial resolutions based on the grid sizes, considering the computational time and accuracy  
171 required for resolving the details of the digital UAV model. The first part was the global domain with a  
172 grid size of 0.23×0.23×0.23 m<sup>3</sup>, providing a lower spatial resolution. The second part was a nested  
173 subdomain within the global domain, specifically defined for the position and dimensions of the  
174 anemometer to simulate the measured velocities. The grid size for this nested subdomain was set at



175  $0.0125 \times 0.0125 \times 0.0125$  m<sup>3</sup>, providing a higher spatial resolution. The total number of grids in the  
176 computational domain was  $1.113 \times 10^8$ , and the specific grid configurations are shown in the Fig. 2. The  
177 fluid was modeled as air with characteristics of turbulent and laminar flow, with a turbulence intensity  
178 of 0.1% and a turbulence length scale of 0.012 m. The atmospheric pressure was adjusted to 100976.99  
179 Pa and 90017.95 Pa at altitudes of 30 m and 1000 m, respectively, and the atmospheric temperature was  
180 assumed to be 25 °C at both altitudes. The relative humidity at different altitudes was determined based  
181 on the prescribed pressure and temperature corresponding to each altitude. The UAV's airspeed and  
182 aerodynamic angles, including the angle of attack and sideslip, were configured according to the  
183 different flight parameters provided in Table S1 and S2. To represent the rotor digitally, six virtual  
184 cylinders of the same volume were used to encapsulate the six rotors, with their circumferences match  
185 the rotating trajectory of the propeller tip. These virtual cylinders were treated as the rotational regions  
186 in the CFD simulation, with their rotation directions aligned with the actual rotation direction of the  
187 UAV's propellers. The rotation direction from rotor No. 1 to 6 was alternately clockwise and  
188 counterclockwise, and the rotation speed for each flight condition was obtained from Table S1 and S2.



189  
190 **Figure 2: Grid configuration of the computational domain.**

191 To ensure relatively accurate simulations, two categories of flow field properties were specified as  
192 computational objectives prior to the start of the simulations, and the simulations were terminated upon  
193 convergence of the simulation results for all objectives. The first category comprised global domain  
194 computational objectives, including average total pressure ( $P_G$ ), average velocity ( $V_G$ ), average vertical  
195 velocity ( $V_{Gz}$ ), and average forward velocity ( $V_{Gx}$ ), where the subscript  $G$  denotes the global domain.





196 The second category consisted of subdomain computational objectives, which included the average  
197 velocity ( $V_s$ ), three-dimensional average speed components  $V_{S_x}$ ,  $V_{S_y}$  and  $V_{S_z}$  at the anemometer position  
198 in the simulation coordinate system.

199 Upon simulation completion, these velocity components ( $V_{S_x}$ ,  $V_{S_y}$ ,  $V_{S_z}$ ) were further converted to  
200 velocity components at the anemometer sensor position ( $u_{x\_sensor}$ ,  $u_{y\_sensor}$ ,  $u_{z\_sensor}$ ) in the airframe  
201 coordinate according to Eqs. (6)-(8) below. The converted velocities,  $u_{x\_sensor}$ ,  $u_{y\_sensor}$ ,  $u_{z\_sensor}$ , were  
202 subtracted from the wind velocity (denoted as  $u_{x\_air}$ ,  $u_{y\_air}$ , and  $u_{z\_air}$ ) setting for each CFD  
203 simulation, to estimate the false wind signals arising from the induced flow by the UAV rotors, expressed  
204 with  $\Delta u_x$ ,  $\Delta u_y$  and  $\Delta u_z$ , respectively, using Eqs. (9)-(11).

$$205 \quad u_{x\_sensor} = -V_{S_z} \quad (6)$$

$$206 \quad u_{y\_sensor} = V_{S_x} \quad (7)$$

$$207 \quad u_{z\_sensor} = -V_{S_y} \quad (8)$$

$$208 \quad \Delta u_x = u_{x\_sensor} - u_{x\_air} \quad (9)$$

$$209 \quad \Delta u_y = u_{y\_sensor} - u_{y\_air} \quad (10)$$

$$210 \quad \Delta u_z = u_{z\_sensor} - u_{z\_air} \quad (11)$$

211 In other words, the false wind signals  $\Delta u_x$ ,  $\Delta u_y$  and  $\Delta u_z$  are the terms that must be determined and  
212 corrected for in the wind measurements from the UAV.

### 213 **3 Result and Discussion**

#### 214 **3.1 The effect of flight altitude on rotor interference with anemometer measurements**

215 Through simulating the flight of UAV in diverse environmental scenarios (as illustrated by the example  
216 results in Fig. S1), the deceptive signals produced by the UAV rotors on the anemometer at different  
217 altitudes and wind characteristics were captured. Initially, the influence of flight altitude on the false  
218 signals was examined.

219 The simulation results for the UAV anemometer under different wind directions and speeds at the 30 m  
220 and 1000 m altitudes are summarized in Table S3 and S4, respectively. The simulated flight data under  
221 tailwind and headwind conditions were integrated into a unified data set since the UAV flight velocity



222 vector is parallel to the tailwind and headwind velocity vectors during normal flight. The simulated false  
 223 wind signals on the anemometer in the airframe x, y, and z directions, caused by the propeller induced  
 224 airflow under tailwind and headwind conditions, were represented by  $\Delta u_x^{T/HW}$ ,  $\Delta u_y^{T/HW}$ , and  $\Delta u_z^{T/HW}$ ,  
 225 respectively. For the tailwind and headwind datasets, according to the Wilcoxon non-parametric test for  
 226 paired samples (as shown in Table 2), the differences in  $\Delta u_x^{T/HW}$ ,  $\Delta u_y^{T/HW}$  and  $\Delta u_z^{T/HW}$  were not  
 227 significant (Sig. = 0.05) at either the 30 m or the 1000 m altitudes. Therefore, in the presence of tailwind  
 228 or headwind, the interference from the UAV propeller-induced flow on the anemometer measurement  
 229 can be considered independent of the flight altitude in this altitude range.

230 Similarly, the simulated false wind signals on the anemometer in the x, y, and z directions were  
 231 represented by  $\Delta u_x^{CW}$ ,  $\Delta u_y^{CW}$ , and  $\Delta u_z^{CW}$ . The Wilcoxon non-parametric test of paired samples was  
 232 also applied (shown in Table 1) between the two altitudes. No significant differences were found for  
 233  $\Delta u_x^{CW}$ ,  $\Delta u_z^{CW}$  between the two altitudes, but there was an obvious discrepancy for  $\Delta u_y^{CW}$  ( $p=1.5 \times 10^{-5}$   
 234  $< \alpha=0.05$ ) at the two altitudes. This indicates that under cross wind conditions, the disturbances of the  
 235 UAV propeller in the x and z directions of the anemometer are not altitude dependent, but that in the y  
 236 (upward) direction it is necessary to distinguish the altitude.

237 **Table 2: Wilcoxon nonparametric tests for paired samples of false wind velocity signals between 30 m and**  
 238 **1000 m flight altitudes.**

Wind Types	False Wind Signal	Significance	$\alpha$	Test results
Tailwind/Headwind	$\Delta u_x^{T/HW}$	0.93	0.05	No difference
	$\Delta u_y^{T/HW}$	0.72	0.05	No difference
	$\Delta u_z^{T/HW}$	0.21	0.05	No difference
Crosswind	$\Delta u_x^{CW}$	0.36	0.05	No difference
	$\Delta u_y^{CW}$	$1.5 \times 10^{-5}$	0.05	Significant difference
	$\Delta u_z^{CW}$	0.81	0.05	No difference

### 239 3.2 Rotor Interference on Anemometer Measurements

240 The false wind signals ( $\Delta u_x^{T/HW}$ ,  $\Delta u_y^{T/HW}$ , and  $\Delta u_z^{T/HW}$ ) on the anemometer resulting from the UAV  
 241 rotor -induced flows under tailwind and headwind conditions at both flight altitudes were aggregated  
 242 and fitted as dependent variables in a regression using  $u_{x\_sensor}$  as the independent variable as shown

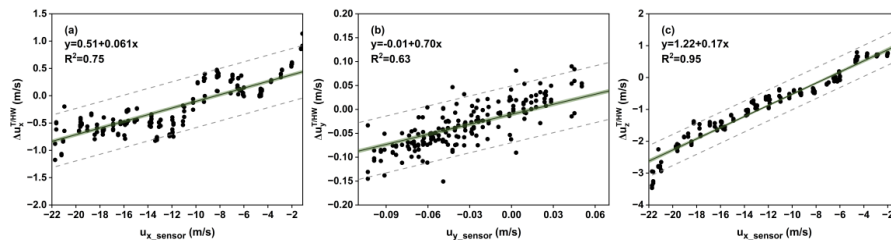


243 in Fig. 3. Good linear relationships  $y=0.51+0.061x$  ( $R^2=0.75$ ),  $y=-0.010+0.70x$  ( $R^2=0.69$ ) and  
 244  $y=1.22+0.17x$  ( $R^2=0.95$ ) were found between  $\Delta u_x^{T/HW}$ ,  $\Delta u_y^{T/HW}$ , and  $\Delta u_z^{T/HW}$  and the simulated  
 245 velocity components in the x-direction ( $u_{x\_sensor}$ ), respectively. Thus, using the UAV velocity  
 246 components in x direction, the false wind signals caused by the UAV propellers can be determined and  
 247 removed from the raw measured wind velocity from the anemometer.

248 For crosswind conditions, regressions were fitted with false wind signals ( $\Delta u_x$  and  $\Delta u_z$ ) as dependent  
 249 variables and  $u_{x\_sensor}$  as the independent variable in the same way (See Fig. 4). A linear relationship  
 250 was observed between the false wind signals in both x and z directions ( $\Delta u_x^{CW}$  and  $\Delta u_z^{CW}$ ) and  $u_{x\_sensor}$ ,  
 251 with the specific expressions  $y = 0.71 + 0.071x$  ( $R^2 = 0.65$ ) and  $y = 0.84 + 0.13x$  ( $R^2 = 0.86$ ), respectively.  
 252 As described in Section 3.1,  $\Delta u_y^{CW}$  was sensitive to flight altitude under crosswind conditions, hence  
 253  $\Delta u_y^{CW}$  at 30 m and 1000 m altitude ( $\Delta u_{y(30)}^{CW}$  and  $\Delta u_{y(1000)}^{CW}$ ) were regressed against  $u_{y\_sensor}$  for the  
 254 two flight altitudes separately. The  $\Delta u_{y(30)}^{CW}$  exhibited a linear relationship with  $u_{y\_sensor}$  ( $y=-$   
 255  $0.0043+0.19x$ ,  $R^2=0.45$ ). However, the correlation coefficient between  $\Delta u_{y(1000)}^{CW}$  and  $u_{y\_sensor}$  was  
 256 found to be lower than 0.5, indicating that  $\Delta u_{y(1000)}^{CW}$  may be considered independent of  $u_{y\_sensor}$ .  
 257 Therefore, the average value of  $\Delta u_{y(1000)}^{CW}$  ( $0.006 \text{ m s}^{-1}$ ) was regarded as the  $\Delta u_{y(1000)}^{CW}$  at this flight  
 258 altitude.

259 Despite the dependence of  $\Delta u_y^{CW}$  on flight altitudes,  $\Delta u_{y(30)}^{CW}$  and  $\Delta u_{y(1000)}^{CW}$  are confined to a similar  
 260 numeric range. Therefore, they may be roughly considered as representing  $\Delta u_y$  for lower altitude (e.g.,  
 261 0 to 500 m) and higher altitude (e.g., 500 to 1000 m), respectively.

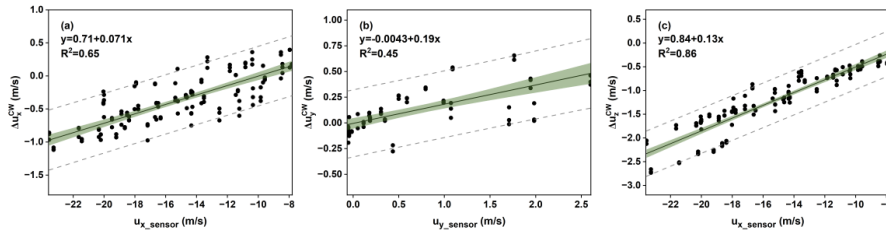
262 Hence, for crosswind situations, the wind velocities in the x, y and z directions measured by the  
 263 anemometer are corrected by subtracting  $\Delta u_x^{CW}$ ,  $\Delta u_y^{CW}$  and  $\Delta u_z^{CW}$  which are estimated from  
 264  $u_{x\_sensor}/u_{y\_sensor}$ , or at relatively high flight altitudes using a constant value of  $0.006 \text{ m s}^{-1}$  for  
 265  $\Delta u_{y(501-1000)}^{CW}$ .



266  
 267 **Figure 3: Regression fit of artificial velocity ( $\Delta u_x^{T/HW}$ ,  $\Delta u_y^{T/HW}$  and  $\Delta u_z^{T/HW}$ ) with  $u_{x\_sensor}$  for tailwind and**  
 268 **headwind flight conditions at two altitudes. In the figure, simulation data are marked with black dots, fitted**



269 curves are indicated in black lines, the 95% confidence bands are identified as green shadows, and the 95%  
 270 prediction bands are represented with gray dashed area.



271  
 272 **Figure 4: Regression fit of false wind velocity signals  $\Delta u_x^{CW}$ ,  $\Delta u_z^{CW}$  and  $\Delta u_y^{CW}$  with  $u_{x\_sensor}/u_{y\_sensor}$**   
 273 **for crosswind flight conditions at two altitudes. The symbols in the figure are the same as in Figure 3.**

### 274 3.3 The Overall Correction Algorithm

#### 275 3.3.1 Motion and Attitude Compensation Correction of UAV

276 In addition to the false wind signals caused by propeller rotations, additional false wind velocity signals  
 277 from the anemometer can be attributed to UAV movement and attitude (pitch, roll and yaw) changes  
 278 during flight, and as such also need correction. When the UAV moves horizontally and vertically relative  
 279 to the ground, the velocity vector measured by the anemometer is a vector combination of the true wind  
 280 velocity and the UAV's ground velocity. Consequently, the ground velocity of the UAV ( $v_x$  and  $v_z$ , with  
 281  $v_y$  always 0 due to no motion in the y direction) contributes false wind velocity components to  
 282 measurements by the anemometer. Moreover, the UAV's flight attitude undergoes adjustments in the  
 283 pitch, roll, and yaw Euler angles ( $\theta$ ,  $\phi$ , and  $\psi$ , respectively), in order to compensate for aerodynamic  
 284 resistance or adapt to flight plans. These adjustments lead to the anemometer measuring additional  
 285 velocities resulting from the rotational rates of the attitude angles ( $\mu(\theta)$  and  $\mu(\phi)$ , with  $\mu(\psi)$   
 286 remaining zero due to the alignment of the rotational axis of  $\psi$  with the line connecting the UAV's center  
 287 of gravity and the anemometer. Furthermore, the effect is further amplified by the distance ( $r$ ) between  
 288 the anemometer and the UAV's center of gravity. It is noteworthy that there is currently no reported  
 289 correction algorithm for influence of attitude angle variations on anemometer wind velocity  
 290 measurements from UAVs. To obtain accurate wind information, after eliminating the aforementioned  
 291 interferences, the wind velocities ( $u_x$ ,  $u_y$  and  $u_z$ ) observed by the anemometer in the airframe coordinate  
 292 ( $x$ ,  $y$  and  $z$  directions) were transformed to the North-East-Down (NED) ground coordinate using the  
 293 direction cosine matrix (DCM) as given in Eq. (12).



$$294 \quad \begin{bmatrix} u_N \\ u_E \\ u_D \end{bmatrix} = \text{DCM}(\theta, \varphi, \psi) \left( \begin{bmatrix} u_x \\ u_y \\ u_z \end{bmatrix} + \begin{bmatrix} v_x \\ 0 \\ -v_z \end{bmatrix} + \begin{bmatrix} \mu(\theta) \\ -\mu(\varphi) \\ 0 \end{bmatrix} \right) \quad (12)$$

$$295 \quad \text{DCM}(\theta, \varphi, \psi) = \begin{bmatrix} \cos(\psi) & -\sin(\psi) & 0 \\ \sin(\psi) & \cos(\psi) & 0 \\ 0 & 0 & 1 \end{bmatrix} \begin{bmatrix} \cos(\theta) & 0 & \sin(\theta) \\ 0 & 1 & 0 \\ -\sin(\theta) & 0 & \cos(\theta) \end{bmatrix} \begin{bmatrix} 1 & 0 & 0 \\ 0 & \cos(\varphi) & -\sin(\varphi) \\ 0 & \sin(\varphi) & \cos(\varphi) \end{bmatrix} \quad (13)$$

296 where DCM is defined by Eq. (13);  $u_N$ ,  $u_E$  and  $u_D$  refer to corrected North, East and Down  
 297 components of wind velocity in the ground coordinate;  $v_x$  and  $v_z$  are the motion velocities of the UAV  
 298 in the x and z directions respectively, which are directly provided by the GPS receiver output of the  
 299 UAV or can be directly computed from the UAV longitude/latitude coordinate output;  $\mu(\theta)$  and  $\mu(\varphi)$   
 300 represent the product of the pitch rate  $\omega(\theta)$  and roll rate  $\omega(\varphi)$ , respectively, with the rotation radius  $r$ ,  
 301 which is the distance between the anemometer and the center of gravity of the UAV, as defined in Eqs.  
 302 (14)-(15). Due to the alignment of the anemometer's z-axis with that of the UAV, the variation in yaw  $\psi$   
 303 does not introduce false wind speed to signals from the anemometer in the airframe coordinate, resulting  
 304 in  $\mu(\psi)$  being equal to zero.

$$305 \quad \mu(\theta) = \omega(\theta) \times r = \frac{d(\theta)}{dt} \times r \quad (14)$$

$$306 \quad \mu(\varphi) = \omega(\varphi) \times r = \frac{d(\varphi)}{dt} \times r \quad (15)$$

307 where  $\omega(\theta)$  and  $\omega(\varphi)$  are defined as the differentiation of  $\theta$  and  $\varphi$  with respect to time  $t$ ,  
 308 respectively.

### 309 3.3.2 Compensation Correction for Induced-Flow Disturbance by UAV Rotor Propellers

310 Based on the statistical analyses of the fluid simulation results in Section 3.2, the regression relationships  
 311 between the false wind velocity signals generated by the propeller rotation and the simulated wind  
 312 components sensed by the anemometer are integrated into the motion and attitude correction algorithm  
 313 of UAV given in Eq. (12). The updated wind velocity correction algorithm is given as Equation 16,  
 314 whose second and third vectors on the right side of Equation 16 represent the contributions of the  
 315 propeller-induced wind signals under tailwind/headwind and crosswind conditions to  $u_x$ ,  $u_y$  and  $u_z$ ,  
 316 respectively, with A and B defined in Eqs. (17)-(18) to quantify their magnitudes. Since the measured  
 317 wind velocities  $u_x$  and  $u_y$  from the anemometer correspond to the simulated  $u_{x\_sensor}$  and  $u_{y\_sensor}$ ,  
 318 respectively, the regression relationships are modified by replacing  $u_x$  and  $u_y$  with  $u_{x\_sensor}$  and  $u_{y\_sensor}$ ,



319 respectively. This yields the estimations of the false wind velocity signals,  $\Delta u_x$ ,  $\Delta u_y$ , and  $\Delta u_z$ , under  
 320 different wind directions, in relation to  $u_x$  and  $u_y$ , as specified by Eqs. (19)-(25). Using Eq. 16, the actual  
 321 wind velocity components, including north wind ( $u_N$ ), east wind ( $u_E$ ), and vertical wind ( $u_D$ ), are  
 322 computed after correcting for the effects of UAV's rotor propeller disturbance, motion, and attitude on  
 323 the wind signal measurements from the anemometer.

$$324 \begin{bmatrix} u_N \\ u_E \\ u_D \end{bmatrix} = \text{DCM}(\theta, \varphi, \psi) \left( \begin{bmatrix} u_x \\ u_y \\ u_z \end{bmatrix} - \begin{bmatrix} A \times \Delta u_x^{T/HW} \\ A \times \Delta u_y^{T/HW} \\ A \times \Delta u_z^{T/HW} \end{bmatrix} - \begin{bmatrix} B \times \Delta u_x^{CW} \\ B \times \Delta u_y^{CW} \\ B \times \Delta u_z^{CW} \end{bmatrix} + \begin{bmatrix} v_x \\ 0 \\ v_z \end{bmatrix} + \begin{bmatrix} -\mu(\theta) \\ \mu(\varphi) \\ 0 \end{bmatrix} \right) \quad (16)$$

$$325 A = \left| \frac{u_x}{\sqrt{u_x^2 + u_y^2}} \right| \quad (17)$$

$$326 B = \left| \frac{u_y}{\sqrt{u_x^2 + u_y^2}} \right| \quad (18)$$

$$327 \Delta u_x^{T/HW} = 0.51 + 0.061 \times u_x \quad (19)$$

$$328 \Delta u_y^{T/HW} = -0.01 + 0.70 \times u_y \quad (20)$$

$$329 \Delta u_z^{T/HW} = 1.22 + 0.17 \times u_x \quad (21)$$

$$330 \Delta u_x^{CW} = 0.71 + 0.071 \times u_x \quad (22)$$

$$331 \Delta u_y^{CW} = -0.0043 + 0.19 \times u_y \quad (h = 0 \sim 500 \text{ m}) \quad (23)$$

$$332 \Delta u_y^{CW} = 0.006 \quad (h = 501 \sim 1000 \text{ m}) \quad (24)$$

$$333 \Delta u_z^{CW} = 0.84 + 0.13 \times u_x \quad (25)$$

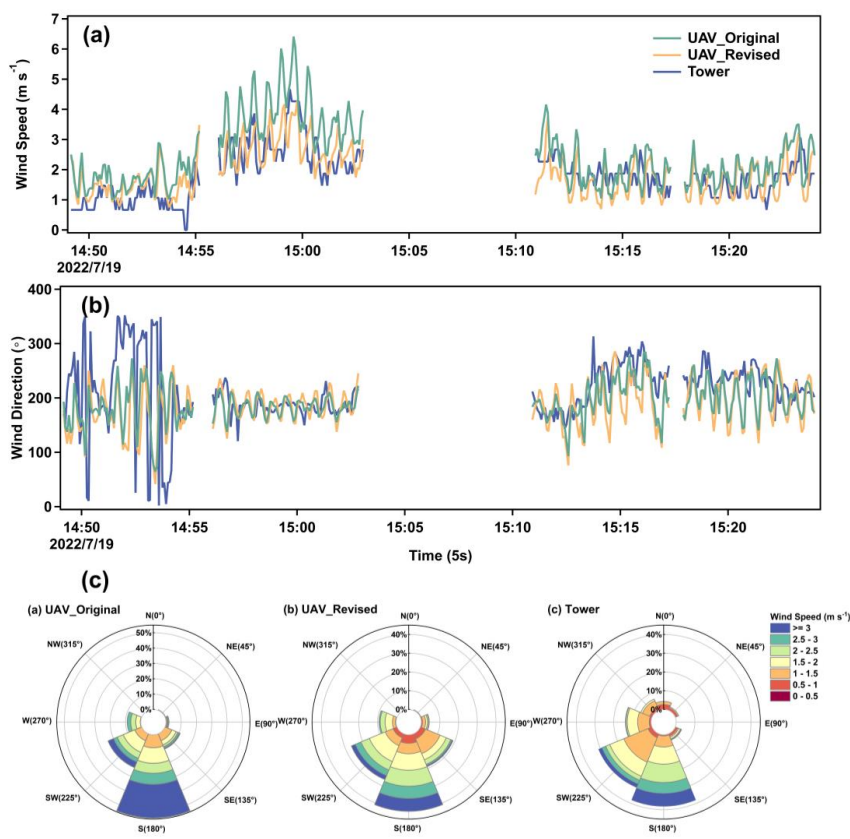
334 In Eqs. (23)-(24), the variable  $h$  represents the flight altitude of the UAV.

### 335 3.4 Validation of the Correction Algorithm

336 To validate the effectiveness of the correction algorithm given by Eq. (16), wind speeds corrected for  
 337 UAV motion and attitude compensation only (Eq. (12) and denoted as UAV\_Original) and the wind  
 338 speeds corrected for rotor disturbance, motion, and attitude compensation (Eq. (16) and denoted as  
 339 UAV\_Revised) were compared with three-dimensional winds measured on an 80-meter meteorological  
 340 tower (denoted as Tower). The comparison experiment was conducted with the UAV flying wind-boxes  
 341 around the meteorological tower within the Experimental Base of the Beijing Key Laboratory of Cloud,



342 Precipitation and Atmospheric Water Resources. The meteorological tower was equipped with three-  
343 dimensional ultrasonic anemometers positioned at heights of 30, 50, and 70 m, with one sensor in the  
344 north and one in the south (see Fig. S2). The UAV flew around the tower in a box flight path at a  
345 horizontal distance of about 10 m away from the tower, at all three heights. Given the potential  
346 interference from near-surface vegetation on the 30-meter anemometer on the tower, wind velocities  
347 acquired by the UAV at 50 and 70 m heights during steady flight intervals were analyzed herein.  
348 The results in Fig. 6(a) demonstrate that at elevated wind speeds ( $>3 \text{ m s}^{-1}$ ), the wind velocities of  
349 UAV\_Revised were substantially lower than UAV\_Original and approximated those from the Tower  
350 more closely. In contrast, under gentle wind speeds ( $\leq 3 \text{ m s}^{-1}$ ), UAV\_Revised exhibited greater  
351 consistency with UAV\_Original but there was still a significant down-revision in the average speed in  
352 UAV\_Revised. The average wind speeds of UAV\_Original, UAV\_Revised, and Tower were 2.4, 1.91,  
353 and  $1.81 \text{ m s}^{-1}$ , respectively, with UAV\_Revised exhibiting a 22% decrease compared to UAV\_Original.  
354 The statistical analysis using the Wilcoxon signed-rank test confirmed a significant difference ( $p < 0.01$ )  
355 in wind speed between UAV\_Original and Tower, whereas no significant differences ( $p > 0.01$ ) were  
356 found between UAV\_Revised and Tower (as shown in Fig.S3). Moreover, under stronger winds, the  
357 wind direction values of UAV\_Revised, UAV\_Original, and Tower were relatively similar, yet at weaker  
358 winds, UAV\_Revised showed a small low-bias (Fig. 5(b)). Compared to UAV\_Original, UAV\_Revised  
359 showed a much improved match between the corrected wind velocity and frequency distributions versus  
360 Tower (Fig. 5(c)), both showing predominant northerly winds. In summary, these analyses indicated that  
361 Eq. 16 can effectively correct wind measurement biases induced by UAV disturbances, motion, and  
362 attitude changes, particularly at higher wind speeds.



363  
364 **Figure 5:** (a) Time-history comparison of wind speed corrected by the UAV compensation algorithm with  
365 those measured by the meteorological tower. (b) Time-history comparison of wind direction corrected by the  
366 UAV compensation algorithm with those measured by the meteorological tower. (c) Comparison of wind  
367 roses between wind corrected by the unmanned aerial vehicle compensation algorithm and those measured  
368 by the meteorological tower. (Note: The meteorological tower measured wind data at 5 s intervals, while the  
369 UAV-based measured and corrected wind data was averaged using a 10 s sliding window before calculating  
370 5 s mean values.)

#### 371 4 Conclusions and Prospective

372 The scenarios involving direct measurements of wind fields within the atmospheric boundary layer using  
373 multirotor UAVs have become progressively commonplace, heightening the significance of accurate  
374 wind assessment. However, the rotor propellers during UAV flight introduce additional induced flows at  
375 the anemometer location, leading to false wind speed signals. For the present UAV-anemometer-payload  
376 configuration, a CFD-based method was used to simulate the process of the UAV wind measurement  
377 platform during stable flights under headwind, tailwind, and crosswind conditions. The analyses of





378 induced airflows surrounding the anemometer led to a predictive tool for disturbance airflows. Building  
379 upon the UAV motion and attitude correction algorithm, a correction algorithm was proposed for the  
380 combined false wind signals from UAV rotor propeller disturbance, motion, and attitude changes during  
381 UAV flights. Through comparison of the corrected wind speeds derived from measurements taken from  
382 the UAV platform and concurrent three-dimensional wind measurements from a nearby meteorological  
383 tower, the validity of the correction algorithm has been demonstrated. This result presents a viable  
384 approach for directly measuring wind speeds with good accuracy from multicopter UAV flights. Indeed,  
385 during the first application of the UAV measurement platform to determine greenhouse gas emission  
386 rates from a large coking plant in one of the largest steelmaker in the country, we have demonstrated that  
387 the emission rates determined on the basis of greenhouse gas concentration and three-dimensional wind  
388 measurements match closely with emission rates determined from material balance (Han T, 2023), again  
389 providing a secondary validation of such a correction algorithm.

390 This research focused on the steady flight state of the UAV. Further research is needed to extend the  
391 correction algorithm to scenarios of UAV ascents, descents, and hovering. Our preliminary assessment  
392 of these scenarios indicate that the correction algorithm is applicable with slightly larger biases based  
393 on limited intercomparison data. In subsequent research, we intend to extend the investigation to  
394 encompass a broader spectrum of UAV flight states, with the objective of achieving a more  
395 comprehensive correction algorithm of wind speeds directly measured during diverse flight  
396 circumstances.

397 **Acknowledgment:** This project was supported by a grant from the National Natural Science Foundation  
398 of China Creative Research Group Fund (22221004).

399 **Competing interests:** The contact author has declared that none of the authors has any competing  
400 interests.

#### 401 **Reference**

402 Anderson, K. and Gaston, K. J.: Lightweight unmanned aerial vehicles will revolutionize spatial ecology,  
403 Front. Ecol. Environ., 11, 138-146, <https://doi.org/10.1890/120150>, 2013.

404 Barbieri, L., Kral, S. T., Bailey, S. C. C., Frazier, A. E., Jacob, J. D., Reuder, J., Brus, D., Chilson, P. B.,  
405 Crick, C., Detweiler, C., Doddi, A., Elston, J., Foroutan, H., Gonzalez-Rocha, J., Greene, B. R., Guzman,



406 M. I., Houston, A. L., Islam, A., Kempainen, O., Lawrence, D., Pillar-Little, E. A., Ross, S. D., Sama,  
407 M. P., Schmale, D. G., Schuyler, T. J., Shankar, A., Smith, S. W., Waugh, S., Dixon, C., Borenstein, S.,  
408 and de Boer, G.: Intercomparison of small unmanned aircraft system (sUAS) measurements for  
409 atmospheric science during the LAPSE-RATE campaign, *Sensors* (Basel), 19,  
410 <https://doi.org/10.3390/s19092179>, 2019.

411 Bonin, T. A., Chilson, P. B., Zielke, B. S., Klein, P. M., and Leeman, J. R.: Comparison and application  
412 of wind retrieval algorithms for small unmanned aerial systems, *Geosci. Instrum., Methods Data Syst.*,  
413 2, 177-187, <https://doi.org/10.5194/gi-2-177-2013>, 2013.

414 Booij, N., Ris, R. C., and Holthuijsen, L. H.: A third-generation wave model for coastal regions: 1. Model  
415 description and validation, *J. Geophys. Res.: Oceans*, 104, 7649-7666,  
416 <https://doi.org/10.1029/98JC02622>, 1999.

417 de Divitiis, N.: Wind estimation on a lightweight vertical-takeoff- and-landing uninhabited vehicle, *J.*  
418 *Aircr.*, 40, 759-767, <https://doi.org/10.2514/2.3155>, 2003.

419 Drob, D. P., Emmert, J. T., Meriwether, J. W., Makela, J. J., Doornbos, E., Conde, M., Hernandez, G.,  
420 Noto, J., Zawdie, K. A., McDonald, S. E., Huba, J. D., and Klenzing, J. H.: An update to the Horizontal  
421 Wind Model (HWM): The quiet time thermosphere, *Earth Space Sci.*, 2, 301-319,  
422 <https://doi.org/10.1002/2014EA000089>, 2015.

423 Elston, J., Argrow, B., Stachura, M., Weibel, D., Lawrence, D., and Pope, D.: Overview of small fixed-  
424 wing unmanned aircraft for meteorological sampling, *J. Atmos. Ocean. Technol.*, 32, 97-115,  
425 <https://doi.org/10.1175/Jtech-D-13-00236.1>, 2015.

426 Gonzalez-Rocha, J., Woolsey, C. A., Sultan, C., and De Wekker, S. F. J.: Sensing wind from quadrotor  
427 motion, *J. Guid. Control Dyn.*, 42, 836-852, <https://doi.org/10.2514/1.G003542>, 2019.

428 Gousseau, P., Blocken, B., Stathopoulos, T., and van Heijst, G. J. F.: CFD simulation of near-field  
429 pollutant dispersion on a high-resolution grid: A case study by LES and RANS for a building group in  
430 downtown Montreal, *Atmos. Environ.*, 45, 428-438, <https://doi.org/10.1016/j.atmosenv.2010.09.065>,  
431 2011.

432 Gryning, S. E., Holtslag, A. A. M., Irwin, J. S., and Sivertsen, B.: Applied dispersion modelling based  
433 on meteorological scaling parameters, *Atmos. Environ.*, 21, 79-89, [https://doi.org/10.1016/0004-  
434 6981\(87\)90273-3](https://doi.org/10.1016/0004-6981(87)90273-3), 1987.



- 435 Han T, X. C., Liu Y, Yang Y, Zhang Y, Huang Y, Gao X, Zhang X., Bao F, and Li S-M.: Application of a  
436 new UAV measurement methodology to the quantification of CO<sub>2</sub> and CH<sub>4</sub> emissions from a major  
437 coking plant, *Atmos. Meas. Tech.*, In Prep, 2023.
- 438 Hedworth, H., Page, J., Sohl, J., and Saad, T.: Investigating Errors Observed during UAV-Based Vertical  
439 Measurements Using Computational Fluid Dynamics, *Drones*, 6, 253,  
440 <https://doi.org/10.3390/drones6090253>, 2022.
- 441 Kim, M.-S. and Kwon, B. H.: Estimation of sensible heat flux and atmospheric boundary layer height  
442 using an unmanned aerial vehicle, *Atmosphere*, 10, 363, <https://doi.org/10.3390/atmos10070363>, 2019.
- 443 Langelaan, J. W., Alley, N., and Neidhoefer, J.: Wind field estimation for small unmanned aerial vehicles,  
444 *J. Guid. Control Dyn.*, 34, 1016-1030, <https://doi.org/10.2514/1.52532>, 2011.
- 445 Martin, S., Bange, J., and Beyrich, F.: Meteorological profiling of the lower troposphere using the  
446 research UAV "M<sup>2</sup>AV Carolo", *Atmos. Meas. Tech.*, 4, 705-716, <https://doi.org/10.5194/amt-4-705-2011>,  
447 2011.
- 448 McGonigle, A., Aiuppa, A., Giudice, G., Tamburello, G., Hodson, A., and Gurrieri, S.: Unmanned aerial  
449 vehicle measurements of volcanic carbon dioxide fluxes, *Geophys. Res. Lett.*, 35,  
450 <https://doi.org/10.1029/2007GL032508>, 2008.
- 451 Neumann, P. P. and Bartholmai, M.: Real-time wind estimation on a micro unmanned aerial vehicle  
452 using its inertial measurement unit, *Sens. Actuators, A*, 235, 300-310,  
453 <https://doi.org/10.1016/j.sna.2015.09.036>, 2015.
- 454 Niedzielski, T., Skjøth, C., Werner, M., Spallek, W., Witek, M., Sawiński, T., Drzeniecka-Osiadacz, A.,  
455 Korzystka-Muskała, M., Muskała, P., and Modzel, P.: Are estimates of wind characteristics based on  
456 measurements with Pitot tubes and GNSS receivers mounted on consumer-grade unmanned aerial  
457 vehicles applicable in meteorological studies?, *Environ. Monit. Assess.*, 189, 1-18,  
458 <https://doi.org/10.1007/s10661-017-6141-x>, 2017.
- 459 Nolan, P. J., Pinto, J., Gonzalez-Rocha, J., Jensen, A., Vezzi, C. N., Bailey, S. C. C., de Boer, G., Diehl,  
460 C., Laurence, R., Powers, C. W., Foroutan, H., Ross, S. D., and Schmale, D. G.: Coordinated unmanned  
461 aircraft system (UAS) and ground-based weather measurements to predict Lagrangian coherent  
462 structures (LCSs), *Sensors (Basel)*, 18, <https://doi.org/10.3390/s18124448>, 2018.
- 463 Oktay, T. and Eraslan, Y.: Computational fluid dynamics (Cfd) investigation of a quadrotor UAV



464 propeller, International Conference on Energy, Environment and Storage of Energy, 21-25,  
465 Palomaki, R. T., Rose, N. T., van den Bossche, M., Sherman, T. J., and De Wekker, S. F.: Wind estimation  
466 in the lower atmosphere using multirotor aircraft, *J. Atmos. Ocean. Technol.*, 34, 1183-1191,  
467 <https://doi.org/10.1175/JTECH-D-16-0177.1>, 2017.  
468 Quan, Q.: Introduction to Multicopter Design and Control, Springer Singapore, 384 pp.,  
469 <https://doi.org/10.1007/978-981-10-3382-7>, 2017.  
470 Rautenberg, A., Graf, M. S., Wildmann, N., Platis, A., and Bange, J.: Reviewing wind measurement  
471 approaches for fixed-wing unmanned aircraft, *Atmosphere*, 9, <https://doi.org/10.3390/atmos9110422>,  
472 2018.  
473 Riddell, K. D. A.: Design, testing and demonstration of a small unmanned aircraft system (SUAS) and  
474 payload for measuring wind speed and particulate matter in the atmospheric boundary layer, University  
475 of Lethbridge, Canada, 2014.  
476 Rogers, K. and Finn, A.: Three-dimensional UAV-based atmospheric tomography, *J. Atmos. Ocean.*  
477 *Technol.*, 30, 336-344, <https://doi.org/10.1175/JTECH-D-12-00036.1>, 2013.  
478 Seibert, P., Beyrich, F., Gryning, S. E., Joffre, S., Rasmussen, A., and Tercier, P.: Review and  
479 intercomparison of operational methods for the determination of the mixing height, *Atmos. Environ.*, 34,  
480 1001-1027, [https://doi.org/10.1016/S1352-2310\(99\)00349-0](https://doi.org/10.1016/S1352-2310(99)00349-0), 2000.  
481 Shaw, J. T., Shah, A. D., Yong, H., and Allen, G.: Methods for quantifying methane emissions using  
482 unmanned aerial vehicles: a review, *Philos. T. Roy. Soc. A*, 379, <https://doi.org/10.1098/rsta.2020.0450>,  
483 2021.  
484 Shimura, T., Inoue, M., Tsujimoto, H., Sasaki, K., and Iguchi, M.: Estimation of wind vector profile  
485 using a hexarotor unmanned aerial vehicle and its application to meteorological observation up to 1000  
486 m above surface, *J. Atmos. Ocean. Technol.*, 35, 1621-1631, [https://doi.org/10.1175/JTECH-D-17-](https://doi.org/10.1175/JTECH-D-17-0186.1)  
487 [0186.1](https://doi.org/10.1175/JTECH-D-17-0186.1), 2018.  
488 Soddell, J. R., McGuffie, K., and Holland, G. J.: Intercomparison of atmospheric soundings from the  
489 Aerosonde and radiosonde, *J. Appl. Meteorol.*, 43, 1260-1269, [https://doi.org/10.1175/1520-](https://doi.org/10.1175/1520-0450(2004)043<1260:IOASFT>2.0.CO;2)  
490 [0450\(2004\)043<1260:IOASFT>2.0.CO;2](https://doi.org/10.1175/1520-0450(2004)043<1260:IOASFT>2.0.CO;2), 2004.  
491 Spiess, T., Bange, J., Buschmann, M., and Vorsmann, P.: First application of the meteorological Mini-  
492 UAV 'M<sup>2</sup>AV', *Meteorol. Z.*, 16, 159-170, <https://doi.org/10.1127/0941-2948/2007/0195>, 2007.



493 Stewart, M., Martin, S., and Barrera, N., Barrera, N. (Ed.): Unmanned aerial vehicles: fundamentals,  
494 components, mechanics, and regulations, Unmanned Aerial Vehicles, Nova Science Publishers,  
495 Hauppauge, New York, USA, 71 pp, 2021.

496 Stockie, J. M.: The mathematics of atmospheric dispersion modeling, SIAM Rev., 53, 349-372,  
497 <https://doi.org/10.1137/10080991X>, 2011.

498 Thielicke, W., Hubert, W., Muller, U., Eggert, M., and Wilhelm, P.: Towards accurate and practical  
499 drone-based wind measurements with an ultrasonic anemometer, Atmos. Meas. Tech., 14, 1303-1318,  
500 <https://doi.org/10.5194/amt-14-1303-2021>, 2021.

501 van Hooff, T. and Blocken, B.: Coupled urban wind flow and indoor natural ventilation modelling on a  
502 high-resolution grid: A case study for the Amsterdam ArenA stadium, Environ. Model. Softw., 25, 51-  
503 65, <https://doi.org/10.1016/j.envsoft.2009.07.008>, 2010.

504 Vardoulakis, S., Fisher, B. E. A., Pericleous, K., and Gonzalez-Flesca, N.: Modelling air quality in street  
505 canyons: a review, Atmos. Environ., 37, 155-182, [https://doi.org/10.1016/S1352-2310\(02\)00857-9](https://doi.org/10.1016/S1352-2310(02)00857-9),  
506 2003.

507 Villa, T. F., Gonzalez, F., Miljevic, B., Ristovski, Z. D., and Morawska, L.: An overview of small  
508 unmanned aerial vehicles for air quality measurements: Present applications and future prospectives,  
509 Sensors (Basel), 16, <https://doi.org/10.3390/s16071072>, 2016.

510